ChemComm

Electrical Monitoring of Human-serum-albumin-templated Molecularly Imprinted Polymer Nanoparticles with High Affinity Based on Molecular Charges and Its Visualization

Journal:	*ChemComm*
Manuscript ID	CC-COM-07-2024-003541.R1
Article Type:	Communication

ChemComm

COMMUNICATION

Electrical Monitoring of Human-serum-albumin-templated Molecularly Imprinted Polymer Nanoparticles with High Affinity Based on Molecular Charges and Its Visualization

Received 00th January 20xx,
Accepted 00th January 20xx

DOI: 10.1039/x0xx00000x

Youyuan Man,[a] Shoichi Nishitani,[b] Kazuaki Sawada [c] and Toshiya Sakata [*a]

Human-serum-albumin (HSA)-templated molecularly imprinted polymer nanoparticles (nano-MIPs) were integrated with a solution-gated field-effect transistor-based biosensor. The real-time electrical analysis of nano-MIP–HSA binding showed a high affinity and specificity of nano-MIPs for HSA. Moreover, the binding behaviour was continuously visualised using a solution-gated complementary metal-oxide semiconductor array image biosensor.

Biosensors consist of a receptor to identify a target, a transducer to convert the receptor–target interaction into an electrical signal, and an output system to process the signal.[1] Among transducers, field-effect transistors (FETs) can detect changes in the surface potential due to the receptor–analyte interactions owing to the metal-oxide semiconductor FET (MOSFET) structure. A platform based on a solution-gated FET, which originates from electronics, is suitable for use in miniaturized and cost-effective systems to directly measure biological samples as the FET biosensor in the field of *in vitro* diagnostics.[2] Such miniaturized electronic devices can be easily equipped with a wireless function and attached to the body, which is applicable to wearable biosensors to detect biomarkers in tears, sweat, and saliva, that is, for diagnostics in a blood-sampling-free manner. The prototype of a FET biosensor, which often comes from an ion-selective FET (ISFET), employs the MOSFET structure in a wet environment for pH sensing, replacing the metal gate electrode with an electrolyte solution with a reference electrode and then making the oxide serve as the pH-sensitive membrane.[3] Moreover, extended-gate FETs (EGFETs) enable the connection of a single transducer to various electrodes, enhancing the flexibility in designing the electrode materials interacting with an electrolyte solution extended from the MOSFET gate (**Scheme 1**); ionic interactions at the electrode surface induce electrical signals.[4]

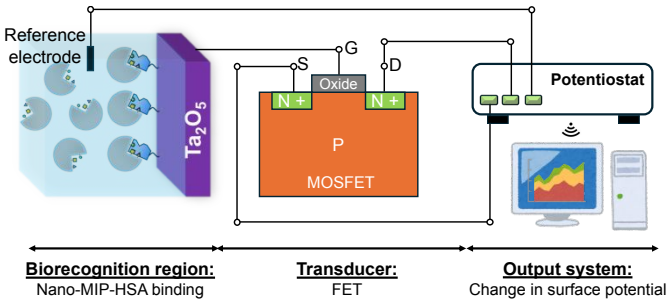

Regarding the receptors, these can be natural or artificial: natural receptors often pose challenges in preservation, production and cost, whereas artificial receptors, although typically have lower affinity, are inexpensive and simpler to produce and preserve.[5] Thus, artificial receptors are always designed such that they emulate the high affinity of natural receptors, such as the antibody–antigen binding.[6] Molecularly imprinted polymers (MIPs) are one of the candidates, selectively capturing their target molecules that serve as templates during their synthesis—a bulk imprinting method.[7,9] This process involves complexing functional monomers and crosslinkers with templates, polymerizing, and then removing the templates to leave cavities that selectively rebind the targets in real samples. However, the bulk imprinting method results in the formation of binding sites with a wide range of affinities; that is, few exhibit tight binding, whereas most have a considerably lower affinity.[10]

To address the bulk imprinting issues, a solid-phase imprinting method has been developed.[11] Here, templates are immobilized onto solid supports like micro-meter glass beads, then contacted with a monomer and crosslinker mixture, forming nano-MIPs with high affinity by initializing the polymerization. These nano-MIPs firmly bind to the template-immobilized supports, whereas subproducts such as unreacted monomers and low-affinity nanoparticles can be washed away. Regarding the collection of synthesized nano-MIPs, a temperature-responsive monomer, n-isopropylacrylamide (NIPAAm), is copolymerized, providing a l ower critical solution temperature (LCST) to the polymer networks.[12,13] When polymerization is completed and the

Scheme 1 EGFET biosensor design: an HSA-immobilized electrode is connected to the gate of a MOSFET. The nano-MIP–HSA binding on the electrode is transmitted to the gate.

[a] *Department of Materials Engineering, School of Engineering, The University of Tokyo, 7-3-1 Hongo, Bunkyo-ku, Tokyo 113-8656, Japan*
[b] *Department of Chemical and Biomolecular Engineering, University of California, Berkeley*
[c] *Department of Electrical and Electronic Information Engineering, Toyohashi University of Technology, 1-1 Hibarigaoka, Tempaku-cho, Toyohashi, Aichi, 441-8580, Japan*

† Electronic supplementary information (ESI) available. See DOI: 10.1039/x0xx00000x

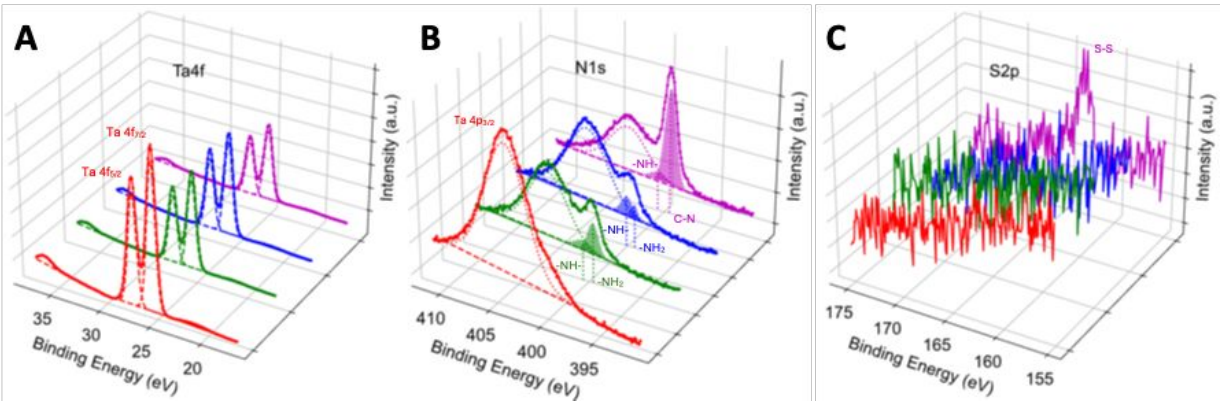

Fig. 1 XPS spectra of (A) Ta 4f, (B) N 1s, and (C) S 2p at each phase before (red) and after (green) polydopamine coating and before (blue) and after (purple) HSA immobilization are presented. In the Ta 4f spectra, the peak intensities of Ta 4f decreased progressively during the modification, especially after HSA immobilization, indicating a layer-by-layer modification. In the N 1s spectra, following the polydopamine coating, an amine peak appeared adjacent to the Ta $4p_{3/2}$ peak. After HSA immobilization, a sharp peak emerged in the N 1s spectra, representing the C–N bond in the polypeptide backbone. In the S 2p spectra, no peak was observed until HSA immobilization, consistent with HSA containing 17 disulfide bonds.

temperature is raised above the LCST, the polymer networks shrink, releasing the nano-MIPs from the template-immobilized solid phases. Nano-MIPs synthesized this way are virtually template-free and maintain high binding affinity, as compared with bulk imprinting. Several instances of successful synthesis of nano-MIPs templating proteins or epitopes have been reported.[14,15]

As our target, human serum albumin (HSA) is selected. This is because HSA plays a crucial role in determining glycated albumin percentage (%GA), which is a biomarker for monitoring blood glucose levels and assessing glycemic control in diabetes patients. %GA reflects blood glucose levels over the previous 21 days,[16] which is more effective in monitoring short-to-middle-term swings glycated hemoglobin percentage (%HbA1c), which reflects blood glucose levels over the previous 120 days.[17,18] We will imprint both HSA and GA, but mainly focus on imprinting HSA in this study because HSA resembles GA (precursor of the glycation process) and thus guides the way for imprinting GA in the future.

In our previous work, we evaluated the fundamental properties of synthesized HSA-templated nano-MIPs.[19] The nano-MIPs were characterized as all-monomer-integrated, uniformly sized, and nanostructured, and they exhibited sufficient affinity and specificity towards HSA. Three monomers were used in the synthesis: NIPAAm, N-tert-butylacrylamide (TBAAm), and acrylamide (AAm). TBAAm and AAm were characterized by attenuated total reflection-Fourier transform infrared spectroscopy, whereas NIPAAm was identified by its swelling behaviour in an aqueous solution. In dynamic light scattering measurements, the polydispersity index and hydrodynamic diameter of nano-MIPs were determined to be 0.30 ± 0.02 and 245 ± 7 nm, respectively, exhibiting their uniformly sized feature. By atomic force microscopy, we confirmed the nanostructure of the nano-MIPs with a spherical morphology. Moreover, the average size in the dry state was determined to be 100 nm by obtaining a histogram. The dissociation constant (K_d) was determined to be 2.4×10^{-9} M by using surface plasmon resonance, exhibiting a high affinity; moreover, specificity was also confirmed.

In this study, we clearly demonstrated the electrical monitoring of the HSA-templated nano-MIP–HSA interaction with the solution-gated FET for the miniaturized electronic system. Here, HSA was immobilized on the extended-gate Ta_2O_5 electrode, where the nano-MIPs were electrically detected as the change in the surface potential of the FET.

Regarding the preparation of the electrodes, Ta_2O_5 was used as a gate material owing to its high-κ dielectricity with a low leakage current.[20] Subsequently, a simple polydopamine coating approach to introduce amine groups proposed by Lee et al. was inspired by the attachment of mussels to wet surfaces.[21] Finally, HSA was crosslinked using glutaraldehyde (**Fig. S1**). To validate the modification methods at each step, substrates before and after polydopamine coating and before and after HSA immobilization were evaluated by X-ray photoelectron spectroscopy (XPS) focusing on Ta 4f, N 1s, and S 2p spectra (**Fig. 1**). The Ta 4f spectrum has well-separated components of Ta $4f_{7/2}$ and Ta $4f_{5/2}$ with an energy separation of 1.9 eV, peaking at 26.2 eV for Ta $4f_{7/2}$ (**Fig. 1A**).[22] Overall, peak intensities decreased as the modification proceeded, especially after HSA immobilization, indicating that a layer-by-layer modification occurred. The peak is still present after dopamine coating, implying two possibilities: (1) X-rays penetrating through a firm polydopamine layer that is probably thin, so X-rays can penetrate; (2) the polydopamine layer with an island structure. Ta $4p_{3/2}$ peaks but overlaps in the N 1s spectrum (**Fig. 1B**),[23] which is evidence of the modification process with a similar trend, aligning with Ta 4f spectra. After the polydopamine coating, the amine peaked adjacent to the Ta $4p_{3/2}$ peak. Gaussian functions were fitted to this peak, with the best fit resulting in peaks at binding energies of 399.7 and 400.6 eV assigned to primary and secondary amines, respectively, indicating that intramolecular cyclization occurred through oxidative dopamine polymerization.[24] After treating the substrates with glutaraldehyde, the best fit was found to differ from the previous step. The intensity of the primary amine peak decreased, indicating changes in chemical states, whereas primary amines linked with glutaraldehyde and turned into

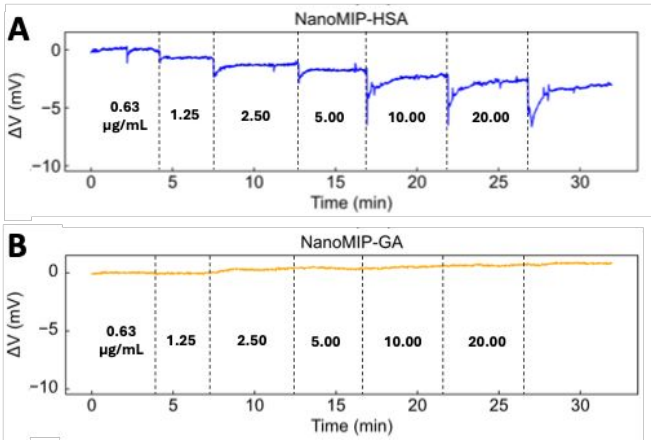

Fig. 2 Sensorgrams of (A) nano-MIP–HSA; (B) nano-MIP–GA binding. The devices with HSA-immobilized electrode produced signals with the output signal decreasing as the nano-MIP concentration increased, whereas the GA-immobilized (positive control) produced noisy signals or maintained silence, indicating that the binding between nano-MIPs and HSA caused ionic events to occur at the gate electrodes.

secondary amines; that is, the area ratio for the two peaks ($S_{\text{-NH}_2}$/ $S_{\text{-NH-}}$) was decreased from 2.26 to 0.43 owing to the anchoring of glutaraldehyde at the polydopamine surface. After HSA immobilization, a sharp peak emerged, representing C–N (399.5 eV) in the polypeptide backbone. In the S 2p spectra, no peak emerged until HSA immobilization: HSA comprises 17 disulfide bonds.[25]

The detection of nano-MIP–HSA binding was then recorded. Each experiment was conducted in triplicate to ensure reproducibility. Moreover, GA-immobilized electrodes were prepared for control experiments in the same manner (**Fig. S1**). All electrodes were conditioned to achieve stable baselines for reliable measurements. The binding results in the deviation of the surface potential from the established baseline (the change in the surface potential) through the charge redistribution at the Ta_2O_5 gate surface, which can be recorded by the FET as a measurable response. After the addition of nano-MIPs, the devices with HSA-immobilized electrodes produced signals with the output voltage decreasing as the nano-MIP concentration increased (**Fig. 2A**), whereas the GA-immobilized (positive control) produced noisy signals or maintained silence (**Fig. 2B**). The result indicates that the binding between nano-MIPs and HSA caused ionic redistribution at the HSA-immobilized electrodes. In the voltage–time profiles of the nano-MIP–HSA interaction, after the addition of nano-MIPs, the devices initially showed a strong signal but gradually stabilized followed by a logarithmic delay. This indicates a diffusion-driven process of ionic events at the interface after the nano-MIP addition. The possible mechanisms can be proposed as to how the device produced signals, depending on the charge of the nano–MIPs. Considering that the zeta potential of the nano-MIPs was measured to be -6.3 ± 2.4 mV, the increase in the amount of the negative charges of nano-MIPs is assumed to have induced the negative shift in the surface potential of the HSA-immobilized electrode. In this case, the output signal may have included the change in the surface potential caused by the fact that the binding expelled the positive counterions of HSA, considering a rule of thumb in a zeta potential measurement of nanoparticles.[26] Moreover, our approach to analysing the response curves of nano-MIP–GA (positive control) involved the evaluation of nonspecific adsorption, which did not show significant changes.

As shown in **Fig. 3**, the equilibrium voltages against the HSA concentrations are plotted and then fitted with a Hill–Langmuir isotherm model,[27] which can be expressed as $\Delta V = -\Delta V_{MAX}([c])^n/([([c])^n + (K_d)^n]$, where $[c]$ is the concentration of nano-MIPs, V the change in signal voltage at equilibrium after nano-MIP addition, V_{MAX} the maximum change in voltage signal when the nano-MIPs reach saturation, K_d the dissociation constant, and n the Hill coefficient. The fitting of our data to the Hill–Langmuir isotherm model reveals K_d of 0.20 µg/mL, R^2 of 1.00, and n of 0.84. The R^2 of 1.00 indicates an excellent fit, suggesting that the fitted parameters of the isotherm model can provide meaningful insights related to the binding process. The n being less than 1, that is, 0.84 indicates negative cooperativity in the binding process;[28] that is, the nano-MIPs may have bound to HSA and inhibited the subsequent bindings, which should be attributed to steric hindrance caused by the bound nano-MIPs. The error margins were quantified using the standard deviation and standard error of the mean. However, these error margins appear somewhat high, indicating variability in the data; that is, they are likely to be due to the small signals to begin with and the multiple processing steps of the substrate samples (artifacts are unavoidable). Additionally, the p-value of 0.01 ($p < 0.05$) demonstrated that the observed differences between the datasets of the target and control sensors within the measured concentrations were statistically significant. The criteria were based on the consistency of the results across replicates; therefore, the errors were considered acceptable if they did not alter the overall trends and conclusions drawn from the data.

On the basis of the concept of FET biosensors, a complementary metal oxide semiconductor (CMOS) array of image sensors revolutionizes image recording technology and have found applications in biosensing technologies. A CMOS image sensor typically consists of a two-dimensional array of

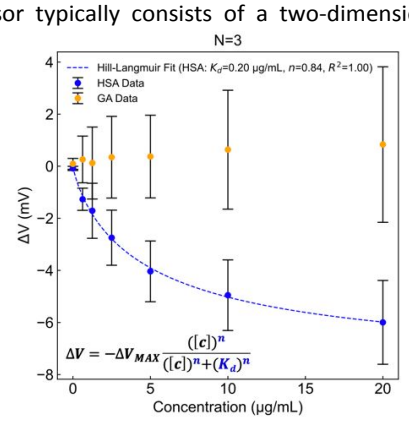

Fig. 3 Hill–Langmuir isotherm fitting of the voltage output values of the HSA-immobilized electrodes in the devices. The fitting of our data to the Hill–Langmuir isotherm reveals a K_d of 0.20 µg/mL and a n of 0.84. The n being 0.84 less than 1 indicates negative cooperativity in the binding process: nano-MIPs bind HSA and inhibit the subsequent bindings, which is attributed to the steric hindrance caused by the bound nano-MIPs. Error bars represent the standard deviation determined from the number of experiments (N = 3).

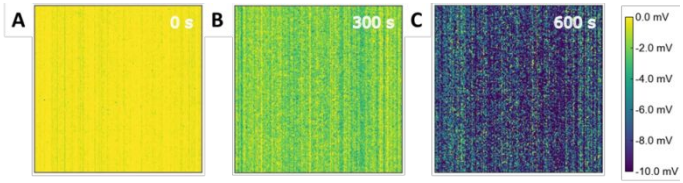

Fig. 4 Visualization (heatmaps) of the real-time nano-MIP–HSA binding of HSA-immobilized CMOS array biosensor (A) at 0 s, (B) at 300 s (with 10 μg/mL nano-MIPs), and (C) at 600 s (with 20 μg/mL of nano-MIPs). This movie is included in Supplementary Information (**Fig. S6**).

pixels (i.e., Ta_2O_5 gate electrodes) arranged in sequential rows and columns (**Fig. S2**).[29] The operation of a pixel in an HSA-immobilized CMOS image sensor possibly involves the following steps; (1) the nano-MIP–HSA binding induces the change in the amount of molecular charges at the surface, (2) this contributes to the formation of a potential well, and (3) the change in surface potential, which is correlated with the potential well, is measured. The variation in the depth of the potential well indicates the amount of nano-MIP–HSA binding at the surface.

The capability of the biosensor to image the nano-MIP–HSA binding on the functionalized CMOS array biosensor was tested. The signals were then used to construct two-dimensional heatmap images, as shown in **Fig. 4**. As the nano-MIPs were added to the HSA-immobilized CMOS array biosensor at 0 s (**Fig. 4A**), the images turned light green at 300 s (**Fig. 4B**) and then dark green at 600 s (**Fig. 4C**). This indicates that the amount of negative charges at the array surface increased owing to the nano-MIP–HSA binding. These results align well with the results obtained using the EGFET sensors (**Figs. 2** and **3**).

In summary, we primarily focused on integrating the synthesized HSA-templated nano-MIPs with the EGFET electrodes. We developed a simple polydopamine coating method to crosslink HSA on the Ta_2O_5 gate electrode, which was characterized by XPS. Real-time analysis showed the interactions between the nano-MIPs and HSA immobilized on the Ta_2O_5 gate electrode of the EGFET sensor. The output signals were then fitted with the Hill–Langmuir isotherm model, obtaining a K_d of 0.20 μg/mL and the Hill coefficient of 0.84, indicating the negative cooperativity in the binding process owing to steric hindrance caused by the nano-MIPs. Furthermore, the capability of the biosensor to image the nano-MIP–HSA binding of the HSA-immobilized CMOS array biosensor was tested. As a result, the functionalized CMOS array biosensor was found to be capable of visualizing the nano-MIP–HSA binding on the basis of the change in the amount of molecular charges. Considering the above, the electrical detection of the nano-MIP–HSA binding shown in this study will contribute to the quantitative analysis of HSA included in biological samples on the basis of a competitive method in the future. In particular, this study indicates the potential use of nano-MIPs in the miniaturized electronic devices with FET biosensors and other future biosensing applications.

This work was financially supported by Program on Open Innovation Platform with Enterprises, Research Institute and Academia (OPERA) of Japan Science and Technology Agency (JST).

Data availability

The data supporting this article have been included as part of the ESI.†

Conflicts of interest

There are no conflicts to declare.

Notes and references

1 D. R. Thévenot, K. Toth, R. A. Durst and G. S. Wilson, Biosens. Bioelectron., 2001, **16**, 121–131.
2 T. Sakata, ACS Omega, 2019, **4**, 11852–11862.
3 P. Bergveld, IEEE Trans. Biomed. Eng., 1972, **19**, 342–351.
4 Ž. Janićijević, T.-A. Nguyen-Le and L. Baraban, Next Nanotechnology, 2023, **3**, 100025.
5 M. Moo-Young and T. Kobayashi, Can. J. Chem. Eng., 1972, **50**, 162–167.
6 T. Sakata, Commun. Chem. 2024, **7**, 35.
7 J. J. BelBruno, Chem. Rev., 2019, **119**, 94–119.
8 X. Zhang, M. Zhu and S. Li, J. Inorg. Organomet. Polym. Mater., 2014, **24**, 890–897.
9 T. Sakata, S. Nishitani and T. Kajisa, RSC Adv., 2020, **10**, 16999–17013.
10 S. C. Zimmerman and N. Gabriel Lemcoff, Chem. Commun., 2004, **1**, 5–14.
11 F. Canfarotta, A. Poma, A. Guerreiro and S. Piletsky, Nat. Protoc., 2016, **11**, 443–455.
12 J. Šťastná, L. Hanyková, Z. Sedláková, H. Valentová and J. Spěváček, Colloid Polym. Sci., 2013, **291**, 2409–2417.
13 H. Yim, M. S. Kent, S. Mendez, S. S. Balamurugan, G. P. Lopez and S. Satija, Macromolecules, 2004, **37**, 1994–1997.
14 M. Chiarello, L. Anfossi, S. Cavalera, F. Di Nardo, T. Serra, F. Sordello and C. Baggiani, J. Mater. Chem. B, 2022, **10**, 6724–6731.
15 F. Canfarotta, L. Lezina, A. Guerreiro, J. Czulak, A. Petukhov, A. Daks, K. Smolinska-Kempisty, A. Poma, S. Piletsky and N. A. Barlev, Nano Lett., 2018, **18**, 4641–4646.
16 P. Rondeau and E. Bourdon, Biochimie, 2011, **93**, 645–658.
17 R. Mahr and J. Frunzke, Appl. Microbiol. Biotechnol., 2016, **100**, 79–90.
18 H. T. Peng, E. Savage, O. Vartanian, S. Smith, S. G. Rhind, C. Tenn and S. Bjamason, J. Clin. Lab. Anal., 2016, **30**, 223–230.
19 Y. Man, S. Nishitani and T. Sakata, Sens. Mater., 2024, accepted.
20 S. Sathasivam, B. A. D. Williamson, A. Kafizas, S. A. Althabaiti, A. Y. Obaid, S. N. Basahel, D. O. Scanlon, C. J. Carmalt and I. P. Parkin, J. Phys. Chem. C, 2017, **121**, 202–210.
21 H. Lee, N. F. Scherer and P. B. Messersmith, Proc. Natl. Acad. Sci. U. S. A., 2006, **103**, 12999–13003.
22 R. A. McLellan, A. Dutta, C. Zhou, Y. Jia, C. Weiland, X. Gui and A. P. M. Place, Chem. Commun., 2023, **10**, 2300921.
23 W. S. Liu, S. H. Huang, C. F. Liu, C. W. Hu, T. Y. Chen and T. P. Perng, Appl. Surf. Sci., 2018, **459**, 477–482.
24 H. A. Lee, E. Park and H. Lee, Adv. Mater., 2020, 32, 1907505.
25 G. Markus and F. Karush, J. Am. Chem. Soc., 1957, **79**, 134–139.
26 J. D. Clogston and A. K. Patri, Methods Mol. Biol., 2011, **697**, 63–70.
27 S. Park, M. Kim, D. Kim, S. H. Kang, K. H. Lee and Y. Jeong, Biosens. Bioelectron., 2020, **147**, 111737.
28 J. N. Weiss, FASEB J., 1997, **11**, 835–841.
29 Y.-N. Lee, T. Araki, Y. Kimura, F. Dasai, T. Iwata, K. Takahashi and K. Sawada, IEEE Trans. Biomed. Circuits Syst., 2019, **13**, 352–363.

Data availability

The data supporting this article have been included as part of the ESI.†